

# Physics-Informed Wireless Imaging with Implicit Neural Representation in RIS-Aided ISAC System

Yixuan Huang<sup>1</sup>, Jie Yang<sup>2,3</sup>, Chao-Kai Wen<sup>4</sup>, Xiao Li<sup>1</sup>, and Shi Jin<sup>1,3</sup>

<sup>1</sup>School of Information Science and Engineering, Southeast University, Nanjing 210096, China

<sup>2</sup>Key Laboratory of Measurement and Control of Complex Systems of Engineering, Ministry of Education, Southeast University, Nanjing 210096, China

<sup>3</sup>Frontiers Science Center for Mobile Information Communication and Security, Southeast University, Nanjing 210096, China

<sup>4</sup>Institute of Communications Engineering, National Sun Yat-sen University, Kaohsiung 80424, Taiwan

Email: {huangyx, yangjie, li\_xiao, jinshi}@seu.edu.cn, chaokai.wen@mail.nsysu.edu.tw

**Abstract**—Wireless imaging is emerging as a key capability in next-generation integrated sensing and communication (ISAC) systems, supporting diverse context-aware applications. However, conventional imaging approaches, whether based on physical models or data-driven learning, face challenges such as accurate multipath separation and representative dataset acquisition. To address these issues, this study explores the use of implicit neural representation (INR), a paradigm that has achieved notable advancements in computer vision, for wireless imaging in reconfigurable intelligent surface-aided ISAC systems. The neural network of INR is specifically designed with positional encoding and sine activation functions. Leveraging physics-informed loss functions, INR is optimized through deep learning to represent continuous target shapes and scattering profiles, enabling resolution-agnostic imaging with strong generalization capability. Extensive simulations demonstrate that the proposed INR-based method achieves significant improvements over state-of-the-art techniques and further reveals the focal length characteristics of the imaging system.

## I. INTRODUCTION

Integrated sensing and communication (ISAC) is one of the primary scenarios for future communication systems [1]. Rather than being confined to locating point targets, ISAC has shown a tendency to sense fine-grained shape and scattering characteristics of extended targets through wireless imaging [2], [3]. Additionally, reconfigurable intelligent surfaces (RISs) have become a key enabler for ISAC to adjust electromagnetic fields, providing diverse sensing perspectives and channel state information (CSI) measurements [4]. This study aims to realize extended target imaging within RIS-aided ISAC systems.

Wireless imaging has been widely studied in literature, where image domain optimization problems are formulated and solved to obtain imaging results. Traditional model-based imaging methods include Fourier transform (FT) and compressed sensing (CS), exhibiting distinct advantages in terms of computational complexity and imaging accuracy. However, both approaches require multipath extraction to retain only the transmitter (TX)-ROI-RIS-receiver (RX) path [5], potentially losing useful information for image generation. Moreover, channel modeling errors may significantly distort the imaging results [3], [6].

In contrast, data-based methods reduce reliance on physical models by learning the relationship between CSI measurements and target images from a large dataset [7]. Although deep learning (DL) techniques have achieved improved imaging performance, constructing such a large dataset is challenging since ground-truth images are difficult to obtain. Furthermore, transferring well-trained model parameters to new imaging scenarios, targets, and resolutions is complicated [8]. While researchers have attempted to integrate physical models into learning [9], these challenges remain inadequately addressed.

Recently, implicit neural representation (INR) has shown excellent performance in computer vision field [10]. Specifically, the term *implicit neural representation* can be decomposed into: 1) *implicit representation*, indicating that INR uses continuous functions to represent sensing results rather than explicit and discretized forms such as images and point clouds, and 2) *neural representation*, meaning that these implicit functions are represented by neural networks (NNs).

In this study, we introduce INR for wireless imaging in RIS-aided ISAC systems, transforming traditional image domain optimization into the optimization of NN parameters, which can be performed using DL techniques under the supervision of differentiable physical models. INR alleviates the need for multipath extraction and does not require ground-truth images or large training datasets, making it significantly superior to traditional model-based and data-based methods. By employing INR, the continuous target shape and scattering characteristics can be learned through NN training, enabling INR to render images of arbitrary resolutions, which is infeasible for state-of-the-art imaging techniques.

## II. SYSTEM MODEL

### A. System Configuration

We consider a RIS-aided ISAC system operating in a 3D space  $[x, y, z]^T \in \mathbb{R}^3$ , as illustrated in Fig. 1. A full-duplex BS is employed to enable both user communication and target imaging. The BS's TX and RX are equipped with uniform linear arrays consisting of  $N_t$  and  $N_r$  antennas, respectively, with half-wavelength spacing  $\lambda/2$ , where  $\lambda$  is the center

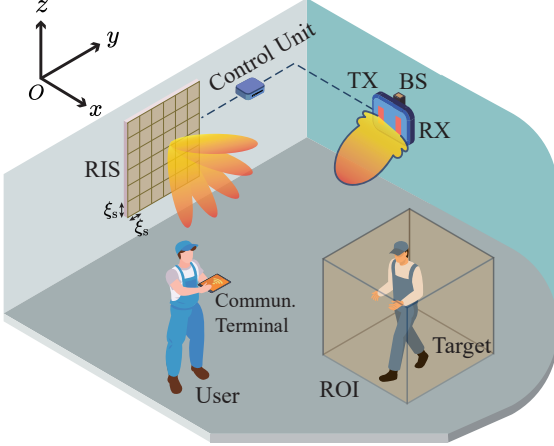


Fig. 1: The proposed RIS-aided ISAC system for wireless imaging.

subcarrier wavelength. Self-interference at the BS is assumed to be mitigated by isolated TX and RX arrays [11]. The RIS is composed of  $N_s$  elements, each with a size of  $\xi_s \times \xi_s$ . Its phase shifts are  $\omega = [\omega_1, \omega_2, \dots, \omega_{N_s}]^T \in \mathbb{C}^{N_s \times 1}$ . The positions of the TX, RX, and RIS are assumed to be known, whereas other environmental components are unknown but considered static.

The region of interest (ROI) is a predefined area where potential targets may be located. It can be divided into  $N_v$  voxels, whose side length is  $\xi_v$ , which is much smaller than  $\lambda/2$  [12], [13]. The ROI image is represented as  $\sigma = [\sigma_1, \sigma_2, \dots, \sigma_{N_v}]^T \in \mathbb{R}^{N_v \times 1}$ , where  $\sigma_{n_v}$  denotes the scattering coefficient of the  $n_v$ -th voxel, and  $\sigma_{n_v} = 0$  if the voxel contains no object. Communication and imaging functions operate in a time-division manner, and  $N_s$  symbol intervals are used to generate ROI images.

### B. Signal and Channel Models

The BS performs target sensing by transmitting signals from the TX and receiving the echoes at the RX. We assume that RIS phases are altered using  $K$  different configurations for imaging, given by  $\Omega = [\omega_1, \omega_2, \dots, \omega_K]^T \in \mathbb{C}^{K \times N_s}$ . While RIS phase optimization for imaging has been studied in [13], this work focuses on imaging algorithm design and assumes that  $\Omega$  is randomly generated in advance. When employing the  $k$ -th RIS configuration  $\omega_k$  and transmitting the  $n_t$ -th signal  $\mathbf{x}_{n_t}$ , the received signal at the RX is expressed as

$$\mathbf{r}_{\text{sen}} = \sqrt{P_t} \mathbf{H}_{\text{sen},k}^T \mathbf{x}_{n_t} + \mathbf{n}_{\text{sen}}, \quad (1)$$

where  $\mathbf{H}_{\text{sen},k} \in \mathbb{C}^{N_t \times N_r}$  denotes the multipath channel between the TX and the RX, and  $\mathbf{n}_{\text{sen}} \in \mathbb{C}^{N_r}$  represents the additive noise at the RX.

According to Fig. 1,  $\mathbf{H}_{\text{sen},k}$  can be expressed as

$$\mathbf{H}_{\text{sen},k} = \mathbf{H}_{\text{tx-roi-rx}} + \mathbf{H}_{\text{tx-ris-rx},k} + \mathbf{H}_{\text{tx-roi-ris-rx},k} + \mathbf{H}_{\text{tx-ris-roi-rx},k} + \mathbf{H}_{\text{others},k}, \quad (2)$$

where  $\mathbf{H}_{\text{tx-roi-rx}}$  and  $\mathbf{H}_{\text{tx-ris-rx},k}$  are the single-bounce paths

scattered by the ROI and RIS, respectively, given by

$$\mathbf{H}_{\text{tx-roi-rx}} = g_{\text{sen}} \mathbf{H}_{\text{tx-roi}} \text{diag}(\sigma) \mathbf{H}_{\text{roi-rx}}, \quad (3a)$$

$$\mathbf{H}_{\text{tx-ris-rx},k} = g_{\text{sen}} \mathbf{H}_{\text{tx-ris}} \text{diag}(\tilde{\omega}_k) \mathbf{H}_{\text{ris-rx}}, \quad (3b)$$

where  $g_{\text{sen}} = \lambda \sqrt{G_{\text{sen}}} / \sqrt{4\pi}$ , and  $G_{\text{sen}}$  is the combined antenna gain of the TX and the RX.  $\mathbf{H}_{\text{tx-roi}}$  and  $\mathbf{H}_{\text{tx-ris}}$  denote the channels from the TX to the ROI and the RIS, respectively.  $\mathbf{H}_{\text{roi-rx}}$  and  $\mathbf{H}_{\text{ris-rx}}$  are the channels from the ROI and the RIS to the RX, respectively. The terms  $\mathbf{H}_{\text{tx-roi-ris-rx},k}$  and  $\mathbf{H}_{\text{tx-ris-roi-rx},k}$  represent twice-bounce paths, given by

$$\mathbf{H}_{\text{tx-roi-ris-rx},k} = g_{\text{sen}} \mathbf{H}_{\text{tx-roi}} \text{diag}(\sigma) \mathbf{H}_{\text{roi-ris}} \text{diag}(\tilde{\omega}_k) \mathbf{H}_{\text{ris-rx}}, \quad (4a)$$

$$\mathbf{H}_{\text{tx-ris-roi-rx},k} = g_{\text{sen}} \mathbf{H}_{\text{tx-ris}} \text{diag}(\tilde{\omega}_k) \mathbf{H}_{\text{ris-roi}} \text{diag}(\sigma) \mathbf{H}_{\text{roi-rx}}, \quad (4b)$$

where  $\mathbf{H}_{\text{roi-ris}} = \mathbf{H}_{\text{ris-roi}}^T$  is the channel between the RIS and the ROI.  $\mathbf{H}_{\text{others},k}$  includes multipaths involving more than two bounces or scatterers beyond the ROI and RIS, representing the unknown portion of the sensing channel  $\mathbf{H}_{\text{sen},k}$ . The next section aims to retrieve  $\sigma$  from the measurements of  $\mathbf{H}_{\text{sen},k}$ .

### III. INR-BASED WIRELESS IMAGING

This section first presents the INR-based imaging algorithm design, and then compares it with traditional model-based and data-driven imaging methods.

#### A. CSI Measurements and Forward Model

INR is developed under the supervision of CSI measurements and forward models. This subsection explains how both components are obtained in the considered ISAC system.

1) *CSI Measurements*: In this study,  $\mathbf{H}_{\text{sen},k}$  is first estimated before performing imaging. Using the least squares (LS) channel estimation algorithm,  $N_t$  received signals are required to derive the estimated CSI, which is given as

$$\hat{\mathbf{H}}_{\text{sen},k} = \mathbf{H}_{\text{sen},k} + \mathbf{N}_{\text{sen},k}, \quad (5)$$

where  $\mathbf{N}_{\text{sen},k}$  denotes the channel estimation error. As a result,  $N_s = KN_t$  symbol intervals are used to acquire sufficient CSI measurements  $\{\hat{\mathbf{H}}_{\text{sen},k}\}_{k=1}^K$  for target imaging, corresponding to the  $K$  varying RIS phase configurations. By stacking all elements in  $\{\hat{\mathbf{H}}_{\text{sen},k}\}_{k=1}^K$ , we derive the measurement vector  $\mathbf{y} \in \mathbb{C}^{N_m \times 1}$  with the dimension of  $N_m = KN_t N_r$ . In contrast to prior studies [5], [13], this approach eliminates the need for multipath extraction and simplifies system design.

2) *Forward Model*: The physical relationship between CSI measurements and the ROI image must be leveraged to impose constraints during image reconstruction. We assume that all point-to-point channels remain constant under the quasi-static condition. In (2),  $\mathbf{H}_{\text{others},k}$  is treated as disturbance to a partially known physical model [5], [13]. Accordingly, (5) can be reformulated as

$$\hat{\mathbf{H}}_{\text{sen},k} = \mathbf{H}'_{\text{sen},k} + \mathbf{N}'_{\text{sen},k}, \quad (6)$$

where

$$\mathbf{H}'_{\text{sen},k} = \mathbf{H}_{\text{tx-roi-rx}} + \mathbf{H}_{\text{tx-ris-rx},k} + \mathbf{H}_{\text{tx-roi-ris-rx},k} + \mathbf{H}_{\text{tx-ris-roi-rx},k},$$

$$\mathbf{N}'_{\text{sen},k} = \mathbf{H}_{\text{others},k} + \mathbf{N}_{\text{sen},k}. \quad (7)$$

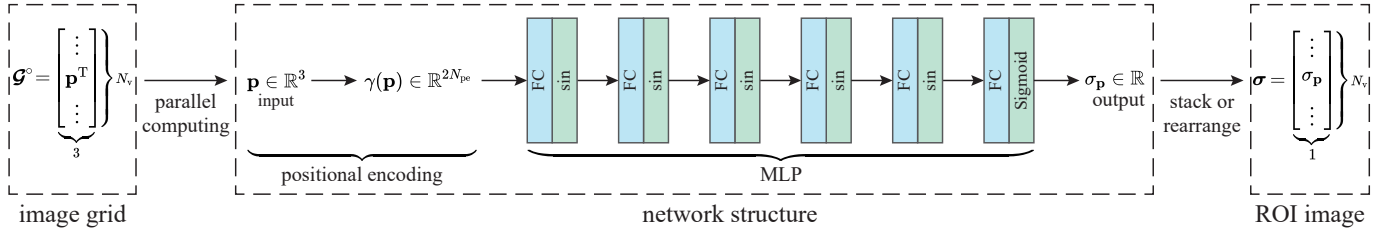


Fig. 2: Illustration of the INR network structure and the relationship between the image grid and the ROI image.

Consequently, the forward model corresponding to the  $k$ -th RIS configuration  $\omega_k$  is expressed as  $f_k(\sigma, \omega_k) = \text{vec}(\mathbf{H}'_{\text{sen},k})$ , where  $\text{vec}(\cdot)$  denotes the vectorization of a matrix. By stacking all  $K$  components  $\{f_k(\sigma, \omega_k)\}_{k=1}^K$ , the complete forward model is denoted as  $f(\sigma, \Omega)$ .

### B. Network Structure

INR employs an NN to learn the representation of the continuous shape and scattering characteristics of the ROI image. Following advanced DL methods [10], the input to the INR is any position  $\mathbf{p} = [x, y, z]^T$  within the ROI, and its output is the corresponding image parameter at that location, i.e., the scattering coefficient at  $\mathbf{p}$ , denoted as  $\sigma_{\mathbf{p}} \in \mathbb{R}$ . Let the INR be denoted by  $\mathcal{M}_{\theta}$  with trainable parameters  $\theta$ ; then, we have

$$\mathcal{M}_{\theta} : \mathbf{p} \longrightarrow \sigma_{\mathbf{p}}. \quad (8)$$

Thus, the continuous ROI image is implicitly stored in  $\mathcal{M}_{\theta}$  through its specific NN architecture and parameters.

We adopt a six-layer multi-layer perceptron (MLP) for the INR, with 256 neurons per layer. However, MLPs tend to exhibit a bias toward learning low-frequency functions, making it difficult to capture high-frequency details presented in ROI images, such as sharp target edges where small movements in position  $\mathbf{p}$  cause significant voxel value changes. To overcome this limitation, we introduce specific positional encoding and a designated activation function to improve the MLP's ability to represent these high-frequency components.

1) *Positional Encoding*: The 3D position  $\mathbf{p}$  is not a suitable direct input to the MLP, since  $\mathbf{p}$  is low-dimensional and lacks high-frequency components beneficial for INR-based imaging. Thus,  $\mathbf{p}$  should be transformed into a higher-dimensional representation that captures more frequency components. This process is referred to as *positional encoding*. In this study, we employ Fourier feature mapping, defined as [14]

$$\gamma(\mathbf{p}) = \begin{bmatrix} \cos(2\pi \mathbf{B}\mathbf{p}) \\ \sin(2\pi \mathbf{B}\mathbf{p}) \end{bmatrix}, \quad (9)$$

where Fourier features are represented by sin and cos functions.  $\mathbf{B} \in \mathbb{R}^{N_{\text{pe}} \times 3}$  is a random Gaussian matrix, with elements independently sampled from a Gaussian distribution  $\mathcal{N}(0, \chi^2)$ . The randomness in  $\mathbf{B}$  enables  $\gamma(\mathbf{p})$  to include components across a broad frequency spectrum. Here,  $N_{\text{pe}}$  is the dimensionality of positional encoding, and  $\chi$  is a hyperparameter controlling the variance of the elements in  $\mathbf{B}$ .

2) *Activation Function*: The commonly used rectified linear unit (ReLU) performs poorly in learning high-frequency signals, due to its piecewise linear nature and lack of second-order derivatives. Alternatively, continuous and periodic functions have been shown to be effective as activation functions in INR-based architectures [15]. In this study, we replace ReLU with the sin function to improve the MLP's ability to learn high-frequency content. The  $i$ -th hidden layer can be expressed as

$$\phi_i(\mathbf{x}_i) = \sin(\kappa(\mathbf{W}_i \mathbf{x}_i + \mathbf{b}_i)), \quad (10)$$

where  $\mathbf{x}_i$ ,  $\mathbf{W}_i$ , and  $\mathbf{b}_i$  represent the input, weights, and biases of the  $i$ -th layer, respectively.  $\kappa$  is a hyperparameter controlling the periodicity of the sine activation. As a result, the continuous image features and high-frequency components are better preserved and recovered within the MLP. Moreover, we apply the NN parameter initialization strategy proposed in [15] to tackle the high sensitivity of initialization caused by sine-based non-linearities. Finally, the output layer employs the Sigmoid activation function, and the overall INR network architecture is illustrated in Fig. 2.

### C. NN Training and Image Generation

By storing image information in the NN, INR transforms direct image-domain optimization into parameter-domain optimization, given by

$$(P1) \quad \theta^* = \underset{\theta}{\operatorname{argmin}} E(f(\mathcal{M}_{\theta}(\mathcal{G}^o), \Omega), \mathbf{y}) + \rho(\mathcal{M}_{\theta}(\mathcal{G}^o)),$$

where  $\mathcal{G}^o \in \mathbb{R}^{N_v \times 3}$  denotes the discrete sampling grid of the continuous image.  $\mathcal{M}_{\theta}(\mathcal{G}^o)$  represents the predicted ROI image of the INR, whose corresponding CSI is calculated by  $f(\mathcal{M}_{\theta}(\mathcal{G}^o), \Omega)$ .  $E(f(\mathcal{M}_{\theta}(\mathcal{G}^o), \Omega), \mathbf{y})$  measures the error between  $f(\mathcal{M}_{\theta}(\mathcal{G}^o), \Omega)$  and CSI measurements  $\mathbf{y}$ , and  $\rho(\mathcal{M}_{\theta}(\mathcal{G}^o))$  is the regularization term capturing the image prior. Moreover, Problem (P1) also leverages an implicit image-statistics prior encoded by the NN structure  $\mathcal{M}_{\theta^*}$ , meaning that all position-parameter pairs  $(\mathbf{p}, \sigma_{\mathbf{p}})$  share a common continuous underlying function [10].

The training procedure iteratively follows four steps:

1) *Step 1—NN Inference*: In each epoch, the NN renders the image stored in its parameters. A sampling grid  $\mathcal{G} \in \mathbb{R}^{N_g \times 3}$  is generated in advance, containing  $N_g$  point locations within the ROI. This grid may be generated through uniform or non-uniform sampling in the 3D ROI space. Sampling density can be adapted using priors to form denser grids in regions of

interest or sparser grids in empty areas [10].<sup>1</sup> The NN receives the grid locations  $\mathcal{G}$  as input and outputs the corresponding predicted scattering coefficients:

$$\hat{\sigma}_{\theta} = \mathcal{M}_{\theta}(\mathcal{G}). \quad (11)$$

By rearranging the elements in  $\hat{\sigma}_{\theta}$  based on their spatial positions, an ROI image is generated, whose resolution is determined by the sampling density of  $\mathcal{G}$ .

2) *Step 2—CSI Prediction:* Given the predicted image  $\hat{\sigma}_{\theta}$ , the corresponding CSI is computed using the forward physical model:

$$\hat{y}_{\theta} = f(\hat{\sigma}_{\theta}, \Omega). \quad (12)$$

3) *Step 3—Loss Calculation:* The NN is trained to minimize the discrepancy between the predicted CSI  $\hat{y}_{\theta}$  and the measured CSI  $y$ . The physics-informed loss function is defined as

$$L_{\theta} = \|\hat{y}_{\theta} - y\|_2 + \alpha \|\hat{\sigma}_{\theta}\|_1, \quad (13)$$

where the first term enforces CSI consistency (the data term in (P1)), and the second term is an explicit regularizer promoting sparsity in the ROI image. The hyperparameter  $\alpha$  controls the weight of the sparsity constraint.

4) *Step 4—NN Parameter Update:* The NN parameters are updated according to the gradient of the loss function:

$$\theta \leftarrow \theta - r \nabla_{\theta} L_{\theta}, \quad (14)$$

where  $r$  is the learning rate and  $\nabla_{\theta} L_{\theta}$  denotes the gradient with respect to  $\theta$ . This update can be implemented using standard DL frameworks such as PyTorch or TensorFlow.

In summary, INR performs imaging using only the forward model and CSI measurements, similar to model-based approaches such as FT and CS. However, the optimization of the ROI image is realized through DL techniques, akin to data-driven methods. After the NN is trained, the final ROI image can be rendered by reapplying Step 1 with the desired image grid  $\mathcal{G}^{\circ}$  as input, given as

$$\hat{\sigma} = \mathcal{M}_{\theta^*}(\mathcal{G}^{\circ}). \quad (15)$$

Although the training grid  $\mathcal{G}$  is discretized, the NN implicitly learns and stores a continuous representation of the ROI image. Therefore, INR allows flexible output image resolution by adjusting the sampling density of  $\mathcal{G}^{\circ}$ , which is infeasible for traditional model-based or data-based imaging approaches.

#### D. Comparison with Traditional Imaging Algorithms

The proposed INR-based imager employs DL-based optimization to extract image information from multipath channel responses and is capable of generating super-resolution images using a small number of CSI measurements. In contrast, model-based methods typically require multipath extraction and retrieve images from a single path, often necessitating a large number of measurements while offering limited resolutions [3], [5], [6], [13]. Moreover, INR supports arbitrary

<sup>1</sup>Since INR learns a continuous representation of the image, the final output resolution  $\mathcal{G}^{\circ}$  can be determined without the limitation of the training grid  $\mathcal{G}$ .



Fig. 3: Example images of the synthesized dataset.

differentiable forward models, whereas FT and CS approaches depend on specific model formulations. Additionally, INR-based imaging is achieved via physics-informed loss functions that integrate domain knowledge into learning [9]. INR does not require constructing large datasets or pre-defining sensing targets, making it superior to traditional DL-based methods in terms of data efficiency and generalization [7], [8].

## IV. NUMERICAL RESULTS

### A. Experimental Settings

1) *Simulation Scenario:* We consider the simulation setup illustrated in Fig. 1. The center subcarrier frequency is set to 3 GHz. The TX and RX are ULAs with  $N_t = N_r = 8$  antennas, and their center locations are  $[10\lambda, 10\lambda, 0]^T$  and  $[10\lambda, -10\lambda, 0]^T$ , respectively. The integrated antenna gain  $G_{\text{sen}} = 4$ . The noise power at each RX antenna is set to  $P_n = -110$  dBm. The RIS is deployed in the yOz plane with its center located at  $[0, 0, 0]^T$ , consisting of  $50 \times 50$  elements with size  $\zeta_s = \lambda_0/2$ , resulting in a UPA of side length 1.53 m. We consider a human imaging scenario, in which the ROI is typically assumed to be 2D in the literature [4]. The ROI center is at  $[D, 0, 0]^T$  in the yOz plane with dimensions of  $2\text{m} \times 2\text{m}$ . The ROI is discretized into  $100 \times 100$  pixels, with each pixel sized  $\lambda/5 \times \lambda/5$ .

2) *Dataset Generation:* We employ a human segmentation dataset from TikTok dance videos on Kaggle [16] to simulate human targets in the ROI. 2615 segmented images are extracted, cropped, resized, and converted into grayscale images of size  $100 \times 100$ . Pixel values are normalized to  $[0, 4\pi A^2/\lambda^2]$ , representing the RCS of a voxel with area  $A = \lambda/5 \times \lambda/5$  [13]. These normalized pixel values reflect the scattering characteristics of the corresponding voxels. Examples from the synthesized dataset are shown in Fig. 3. Note that the ground-truth images are not required by the proposed INR-based imaging method; they are used only to generate CSI measurements and evaluate imaging accuracy.

3) *Training Details:* The NN is trained for 5000 epochs with an initial learning rate of  $10^{-3}$ . The learning rate is reduced by 50% if the validation accuracy does not improve for 50 consecutive epochs, and training stops if no improvement is observed over 200 epochs. The positional encoding dimension is set to  $N_{\text{pe}} = 256$ , and the  $\ell_2$ -norm of the NN gradients is clipped to be below 2. Training is performed using the Adam optimizer on an Nvidia 4090 GPU with the PyTorch platform. The training grid  $\mathcal{G}$  is set equal to the output image grid  $\mathcal{G}^{\circ}$ .

4) *Performance Evaluation Metrics:* The following metrics are used to evaluate imaging quality:

(1) **Mean Square Error (MSE):** Measures the per-voxel error between the predicted  $\hat{\sigma}$  and ground truth  $\sigma$ :

$$\text{MSE} = \|\hat{\sigma} - \sigma\|_2^2 / N_v. \quad (16)$$

TABLE I: Imaging results with different system and training settings (unit for time: second).

RIS phase	no RIS	DFT	random	random	random	random
Activation function	sin	sin	<b>ReLU</b>	sin	sin	sin
Positional encoding	✓	✓	✓	✗	✓	✓
$\alpha$	0	0	0	0	<b>0.01</b>	0
MSE	0.2440	0.0019	0.2485	0.0018	0.0012	<b>0.0011</b>
SSIM	0.0625	0.9228	0.1296	0.9427	<b>0.9889</b>	0.9755
Train time (200 epochs)	<b>0.9427</b>	1.0836	1.0057	1.0409	1.0356	1.1073
Imaging result (200 epochs)						
Train time (5,000 epochs)	<b>23.5677</b>	27.0909	/	26.0224	25.8896	27.6816
Imaging result (5,000 epochs)						

**(2) Peak Signal-to-Noise Ratio (PSNR):** Assesses the ratio of the peak signal power to noise:

$$\text{PSNR} = 10 \log_{10} (\sigma_{\max}^2 / \text{MSE}), \quad (17)$$

where  $\sigma_{\max}$  is the maximum voxel value. MSE and PSNR jointly measure pixel-level accuracy.

**(3) Structural Similarity Index Measure (SSIM):** Evaluates the structural similarity between  $\hat{\sigma}$  and  $\sigma$  [4]:

$$\text{SSIM} = \frac{(2\mu_{\sigma}\mu_{\hat{\sigma}} + c_1)(2\theta_{\sigma\hat{\sigma}} + c_2)}{(\mu_{\sigma}^2 + \mu_{\hat{\sigma}}^2 + c_1)(\theta_{\sigma}^2 + \theta_{\hat{\sigma}}^2 + c_2)}, \quad (18)$$

where  $\mu_{\sigma}$  ( $\mu_{\hat{\sigma}}$ ) and  $\theta_{\sigma}^2$  ( $\theta_{\hat{\sigma}}^2$ ) are the mean and variance of  $\sigma$  ( $\hat{\sigma}$ ), respectively, and  $\theta_{\sigma\hat{\sigma}}$  is the covariance between them. Constants  $c_1$  and  $c_2$  follow the default settings in the skimage package. SSIM ranges from 0 to 1, with higher values indicating better visual similarity. Unlike MSE and PSNR, SSIM captures structural and perceptual fidelity, reflecting human visual perception.

## B. Results and Discussions

**1) Imaging Results with Different Systems and Training Settings:** We evaluate the effectiveness of the proposed INR-based imaging algorithm under  $K = 40$  distinct RIS configurations, with  $D = 40\lambda$ . Table I shows that the proposed method performs well, especially when the sinusoidal activation function and positional encoding are used. After 5000 training epochs, the model produces highly accurate images, with SSIM values approaching 0.99. Even trained for 200 epochs in approximately one second, the INR already generates nearly perfect images. In contrast, using the ReLU activation function results in severely distorted images, and omitting positional encoding also degrades PSNR and SSIM performance. Although omitting the RIS simplifies the forward model and slightly speeds up training, the resulting images are ineffective, indicating the importance of diverse CSI measurements enabled by RIS phase control.

Fig. 4 depicts the training and testing PSNRs for the “no RIS” and “ReLU” configurations. Without RIS, training PSNR increases, but testing PSNR remains below 10 dB, implying

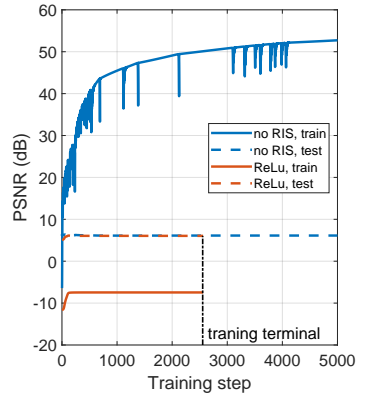


Fig. 4: Train and test PSNR during the training process for “no RIS” and “ReLU” scenarios.

TABLE II: Imaging results using different algorithms. “GT” denotes ground truth.

Algorithm	GT	INR 500	INR 2500	FT 2500	CS 2500
$\xi_v = \lambda/5$					
$\xi_v = \lambda/2.5$					
$\xi_v = \lambda$					

overfitting and poor generalization due to insufficient image information. For the ReLU-based NN, neither training nor testing PSNR improves, indicating that ReLU fails to capture the high-frequency features essential for image reconstruction, despite having access to sufficient CSI data.

**2) Imaging Result Comparison of INR with FT and CS Algorithms:** We compare the imaging performance of FT [5], CS [6], [13], and proposed INR algorithms. To maintain consistent settings, only the TX-ROI-RIS-RX path is employed for imaging, TX and RX antenna numbers are both set to 1, and RIS phases are configured using a DFT codebook. The imaging distance is  $D = 40\lambda$ . As shown in Table II, the proposed INR-based imager significantly outperforms traditional FT and CS methods. With only  $K = 500$  RIS phase variations, INR achieves high imaging quality. In contrast, even with  $K = 2500$  measurements, FT and CS generate degraded images due to strong pixel-wise channel correlations, which limit their ability to resolve fine details. This highlights the advantage of leveraging INR to learn intricate image features directly from CSI data. Furthermore, INR enables the generation of super-resolution images with pixel size  $\xi_v$  much smaller than the resolution limit established in [5]. By comparison, FT and CS can only produce coarse approximations when  $\xi_v = \lambda$ . Therefore, the INR framework presents an effective alternative to conventional model-based imaging approaches, offering enhanced resolution and robustness in

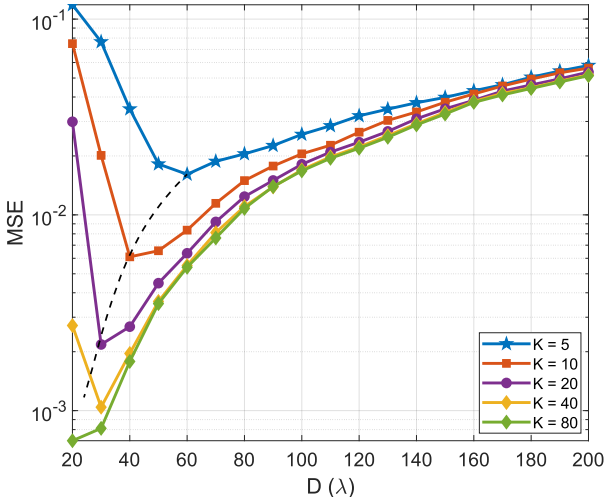


Fig. 5: MSE versus imaging distance and RIS phase variation number.

underdetermined sensing scenarios.

3) *Imaging Performance versus Distance and RIS Phase Variation Number*: This subsection investigates the effects of distance  $D$  and RIS phase variation number  $K$  on imaging quality. The maximum training epoch is set to 1,000. The average MSE for 1,000 images using the proposed INR method are shown in Fig. 5. Several key insights can be drawn.

First, the MSE results indicate that imaging quality initially improves and then degrades as the distance  $D$  increases. This suggests the existence of an optimal imaging distance  $D_0$ , analogous to the focal distance in optical imaging, where performance is maximized. In general,  $D_0$  decreases as  $K$  increases, as illustrated by the dotted black line in Fig. 5. Therefore, collecting more CSI measurements allows the proposed INR-based imager to achieve optimal performance at shorter distances. These findings differ from traditional results [5], [13], which typically conclude that imaging performance deteriorates monotonically with increasing  $D$ .

Second, when  $D < D_0$ , imaging performance is primarily constrained by the number of RIS phase variations  $K$ . In this region, the short imaging distance makes the ROI generate a large field of view to the RIS aperture, requesting a large  $K$  to capture adequate information about the ROI, which resembles the scenario when a man observes a near and large object. As a result, a low  $K$  leads to insufficient sensing perspectives and degraded performance, similar to the no-RIS scenario in Table I. Increasing  $K$  from 5 to 80 can enrich the CSI measurements and ROI-related information, reducing MSE from around  $10^{-1}$  to  $10^{-3}$  at  $D = 20\lambda$ .

Third, when  $D > D_0$ , the influence of  $K$  diminishes. For example, when  $D$  approaches  $200\lambda$ , the MSE values for  $K = 5$  and  $K = 80$  become nearly identical. This indicates that the performance bottleneck shifts from RIS phase diversity to the increasing channel correlations between the RIS and ROI. These correlations make it more difficult to distinguish adjacent pixels as  $D$  increases, consistent with analysis in [5], [13]. Consequently, imaging resolution deteriorates at

larger distances. This condition also shares similarities with optical imaging systems where multiple observation may not significantly improve the resolution at large imaging distances.

## V. CONCLUSION

This study presents a RIS-aided ISAC system in which the communication infrastructure is reused to enable target imaging. The INR technique is innovatively introduced for wireless imaging, where the NN architecture is specifically designed using positional encoding and a sine activation function to embed image information within the NN parameters. Under the supervision of physical models, DL techniques are employed to optimize the image representation, offering several advantages over traditional model-based and data-driven methods. Simulation results demonstrate that the proposed algorithm outperforms state-of-the-art methods by achieving high imaging accuracy with low measurement overhead.

## REFERENCES

- [1] B. Lin *et al.*, “Environment reconstruction based on multi-user selection and multi-modal fusion in ISAC,” *IEEE Trans. Wireless Commun.*, vol. 23, no. 10, pp. 15 083–15 095, Oct. 2024.
- [2] B. Zheng and F. Liu, “Random signal design for joint communication and SAR imaging towards low-altitude economy,” *IEEE Wireless Commun. Lett.*, vol. 13, no. 10, pp. 2662–2666, Oct. 2024.
- [3] Y. Huang, J. Yang, S. Xia, C.-K. Wen, and S. Jin, “Learned off-grid imager for low-altitude economy with cooperative ISAC network,” *IEEE Trans. Wireless Commun.*, early access, Sep. 2025.
- [4] F. Wang, Y. Huang, Z. Feng, R. Xiong, Z. Li, C. Wang, T. Mi, R. C. Qiu, and Z. Ling, “Dreamer: Dual-RIS-aided imager in complementary modes,” *IEEE Trans. Antennas Propag.*, vol. 73, no. 7, pp. 4863–4878, Jul. 2025.
- [5] Y. Huang *et al.*, “Fourier transform-based wavenumber domain 3D imaging in RIS-aided communication systems,” *IEEE Trans. Wireless Commun.*, vol. 23, no. 10, pp. 13 872–13 888, Oct. 2024.
- [6] X. Tong, Z. Zhang, Z. Yang, Y. Ge, and H. Wymeersch, “Computational imaging-based ISAC method with large pixel division,” in *Proc. IEEE Int. Conf. Commun. (ICC)*, Jun. 2025, pp. 1–6.
- [7] B. Lu *et al.*, “Deep learning based multi-node ISAC 4D environmental reconstruction with uplink-downlink cooperation,” *IEEE Internet Things J.*, vol. 11, no. 24, pp. 39 512–39 526, Dec. 2024.
- [8] W. Qi, R. Zhang, J. Zhou, H. Zhang, Y. Xie, and X. Jing, “A resource-efficient cross-domain sensing method for device-free gesture recognition with federated transfer learning,” *IEEE Trans. Green Commun. Networking*, vol. 7, no. 1, pp. 393–400, Mar. 2023.
- [9] R. Guo *et al.*, “Physics-embedded machine learning for electromagnetic data imaging: Examining three types of data-driven imaging methods,” *IEEE Signal Process. Mag.*, vol. 40, no. 2, pp. 18–31, Mar. 2023.
- [10] B. Mildenhall, P. P. Srinivasan, M. Tancik, J. T. Barron, R. Ramamoorthi, and R. Ng, “NeRF: Representing scenes as neural radiance fields for view synthesis,” *Commun. ACM*, vol. 65, no. 1, pp. 99–106, Dec. 2021.
- [11] X. Yang, Z. Wei, J. Xu, H. Wu, and Z. Feng, “Cooperative sensing-assisted predictive beam tracking for MIMO-OFDM networked ISAC systems,” *IEEE Trans. Wireless Commun.*, early access, Jun. 2025.
- [12] N. Mehrotra and A. Sabharwal, “On the degrees of freedom region for simultaneous imaging & uplink communication,” *IEEE J. Sel. Areas Commun.*, vol. 40, no. 6, pp. 1768–1779, Jun. 2022.
- [13] Y. Huang, J. Yang, C.-K. Wen, and S. Jin, “RIS-aided single-frequency 3D imaging by exploiting multi-view image correlations,” *IEEE Trans. Commun.*, vol. 72, no. 8, pp. 5003–5018, Aug. 2024.
- [14] M. Tancik *et al.*, “Fourier features let networks learn high frequency functions in low dimensional domains,” *Adv. Neural Inf. Process. Syst. (NeurIPS)*, vol. 33, pp. 7537–7547, Dec. 2020.
- [15] V. Sitzmann, J. Martel, A. Bergman, D. Lindell, and G. Wetzstein, “Implicit neural representations with periodic activation functions,” *Adv. Neural Inf. Process. Syst. (NeurIPS)*, vol. 33, pp. 7462–7473, 2020.
- [16] K. Roman, “Kaggle dataset: Human segmentation dataset TikTok dances,” [Online]. Available: <https://www.kaggle.com/datasets/tapakah68/segmentation-full-body-tiktok-dancing-dataset>, 2023.